BNL-94881-2012-JA

Aerosol Science and Technology
Publication details, including instructions for authors and subscription information:
http://www.tandfonline.com/loi/uast20

Kinetics of Heterogeneous Nucleation in Supersaturated Vapor: Fundamental Limits to Neutral Particle Detection Revisited

Robert McGraw [a], Jian Wang [a] & Chongai Kuang [a]
[a] Environmental Sciences Department, Atmospheric Sciences Division, Brookhaven National Laboratory, Upton, NY, USA

Available online: 26 Apr 2012

To cite this article: Robert McGraw, Jian Wang & Chongai Kuang (2012): Kinetics of Heterogeneous Nucleation in Supersaturated Vapor: Fundamental Limits to Neutral Particle Detection Revisited, Aerosol Science and Technology, 46:9, 1053-1064

To link to this article: http://dx.doi.org/10.1080/02786826.2012.687844

Aerosol Science and Technology, 46:1053–1064, 2012

ISSN: 0278-6826 print / 1521-7388 online
DOI: 10.1080/02786826.2012.687844

Kinetics of Heterogeneous Nucleation in Supersaturated Vapor: Fundamental Limits to Neutral Particle Detection Revisited

Robert McGraw, Jian Wang, and Chongai Kuang

Environmental Sciences Department, Atmospheric Sciences Division, Brookhaven National Laboratory, Upton, NY

We examine the nucleated (with barrier) activation of perfectly wetting (zero contact angle) particles ranging from essentially bulk size down to approximately 1-nm mass diameter. While similar studies trace back to the pioneering work of Fletcher, we present here a novel approach to the analysis based on general area constructions that enable key thermodynamic properties, including surface and bulk contributions to nucleation work, to be interpreted geometrically with reference to the Kelvin curve. The kinetics of activation are described in more detail in terms of the mean first passage time (MFPT) for barrier crossing. MFPT theory and benchmark calculations are used to develop and test a new approximate-but-simpler-to-use analytic expression for the barrier crossing rate. The present study is motivated by recent condensation particle counter (CPC) studies that appear to finally establish the long-predicted detection of "sub-Kelvin" particles in the nanosize regime. Corresponding states thermodynamic and kinetic scaling approaches are used to facilitate the correlation and selection of optimal CPC working fluids and operating conditions based on a new metric for heterogeneous nucleation, the signal-to-noise ratio, and physical and chemical properties.

[Supplementary materials are available for this article. Go to the publisher's online edition of *Aerosol Science and Technology* to view the free supplementary files.]

1. INTRODUCTION

Striking advance has been made over the past several years in condensation particle counter (CPC) development, enabling particles in the sub-3-nm diameter range approaching the size of molecular clusters to be routinely detected in the laboratory (Winkler et al. 2008; Iida et al. 2009; Sipila et al. 2009; Vanhanen et al. 2011) and in the atmosphere (Jiang et al. 2011). This breakthrough in instrumentation calls for a re-examination of the foundations of the heterogeneous nucleation theory, still largely based on the capillarity approximation (Fletcher 1958), wherein even small clusters are modeled as bulk-property liquid drops with simplified kinetics. Fletcher's theory predicts heterogeneous nucleation, driven by thermal fluctuations, for the activation of very small particles (less than about 6 nm), whereas larger particles undergo a transition to barrierless growth at the Kelvin limit. Activation by nucleation below the Kelvin limit is a key factor in lowering the detectable size, but only recently has the process been definitively observed (Winkler et al. 2008). Another important development has been the screening of multiple CPC working fluids for optimal detector performance in the sub-3-nm regime (Magnusson et al. 2003; Iida et al. 2009).

The present study has several objectives, beginning with re-examination of the theory. Any improvement over Fletcher's analysis is not easily done. One can contemplate a first-principles molecular simulation, but an accurate prediction of nucleation rate requires more realistic model potentials than are presently available. Molecular dynamics and Monte Carlo-based simulations of nucleation, which utilize the model potentials, are particularly useful at establishing trends—e.g., identifying even small systematic departures from the classical nucleation theory—but such simulations are beyond the scope of the present study. Instead, we continue to rely on the capillarity approximation for estimating the thermodynamic properties needed for the theory, while focusing on improving the kinetics. For this, an analysis of the mean first passage times (MFPTs) required for the aggregate of molecular evaporation/condensation growth steps to reach and exceed the size of the critical cluster (consisting of seed particle plus condensate) is presented. Recent results from Wedekind et al. (2007) are extended for this purpose to the kinetics of heterogeneous nucleation. Series expansions for MFPT and nucleation rate are evaluated numerically and used to derive a simple

Received 15 March 2011; accepted 5 March 2012.

This research was supported by the Atmospheric System Research (ASR) Program of the US Department of Energy. Special thanks to Ernie Lewis for valuable discussions and to an anonymous reviewer for a careful and thoughtful review, which greatly helped our presentation of this work.

Address correspondence to Robert McGraw, Environmental Sciences Department, Atmospheric Sciences Division, Brookhaven National Laboratory, Bldg. 815E, Upton, NY 11943, USA. E-mail: rlm@bnl.gov

analytic expression for predicting the heterogeneous nucleation rate. Comparison with the full MFPT calculation shows the approximate formula to be accurate to within a few percentage points for nucleation barrier heights in excess of about 5 kT—a range well covering the region of interest to the present study.

Although physical and chemical properties are derived from the capillarity approximation, a new approach to the thermodynamic analysis is presented. As described in Section 2, the approach is based on graphical constructions derived from the Kelvin curve. There are several reasons for pursuing the new approach: it provides convenient area constructions for homogeneous and heterogeneous nucleation barriers and a graphical interpretation even for key kinetic terms, such as the Zeldovich factor, used in the newly derived rate expression. The method further simplifies the scaling analysis used to correlate working fluid performance in Section 5. Finally, the graphical approach provides a molecular-based framework that recovers results from the classical nucleation theory when the capillarity approximation is used, while retaining applicability even in cases where the classical theory fails (Section 6).

The new results are discussed in the context of early speculations on the application of nucleation and growth as a detection tool for single neutral molecules and clusters (Reiss et al. 1977). A full analysis of detection capability will require, among other considerations, going beyond Fletcher's theory and viewing heterogeneous nucleation as a multi-component molecular interaction process in the nano-size regime. Here, we take preliminary steps in this direction to show that the new formulation provides a molecular-level framework, rooted in mass action and detailed balance, which can be exploited to great advantage in attempts to go beyond the classical nucleation theory.

While the results reported here were in preparation, the authors learned of a similarly motivated study of heterogeneous nucleation, also based on the capillary theory and perfect wetting (Fernandez de la Mora 2011). Although there are similarities between the two studies, there are notable differences in approach. Differences include the introduction here of corresponding states scaling, MFPT kinetics, and novel area constructions that provide a basis for handling the departure from the capillary theory in the form of positive/negative deviations in equilibrium vapor pressure from the Kelvin relation.

2. THERMODYNAMIC AREA CONSTRUCTIONS

This section develops several graphical constructions for key thermodynamic properties that include nucleation barrier height, surface work, and barrier shape. The approach derives from the Kelvin relation, which gives the critical size (generally consisting of seed plus condensed fluid) as a function of vapor saturation ratio:

$$\ln\left(\frac{P_{\rm eq}(g)}{P_{\rm eq}^{\infty}}\right)=\left(\frac{32\pi}{3}\right)^{1/3}\left(\frac{\sigma v_1^{2/3}}{kT}\right)g^{-1/3}. \qquad [1]$$

Here, $g = n_{\rm seed} + n$ is the number of condensed solvent molecules, each of molecular volume v_1, required to fill the total volume, v, consisting of the seed particle volume, $v_{\rm seed} \equiv n_{\rm seed} v_1$, plus the condensate, $v_{\rm cond} = n v_1$. Equivalently, g is the number of liquid-phase condensate molecules present in the same-size homogeneous drop, $v = v_{\rm seed} + v_{\rm cond} = g v_1$. Used here as a continuous parameter, $n_{\rm seed} = v_{\rm seed}/v_1$ refers not to the number of molecules actually present in the seed, but is rather a measure of seed volume. $P_{\rm eq}(g)$ is the vapor pressure in (unstable) equilibrium with the drop, and $P_{\rm eq}^{\infty}$ is the bulk equilibrium vapor pressure over a flat surface. The nondimensional group of physical constants appearing on the right-hand side of Equation (1), which will henceforth be written as $\Omega/T \equiv \sigma v_1^{2/3}/kT$, is a convenient scaling parameter used extensively in the sequel. Here, σ is the bulk surface tension, v_1 is derived from the bulk density, and $\Omega = \sigma v_1^{2/3}/k$ has units of temperature.

Barrier profiles for heterogeneous and homogeneous nucleation may be derived using thermodynamic area constructions similar to those introduced recently to analyze the deliquescence and efflorescence of small particles (McGraw and Lewis 2009). For vapor pressures given by the Kelvin relation, these relations are of the form:

$$\frac{W(n)}{kT}=\int_0^n \ln\left(\frac{P_{\rm eq}(n')}{P_{\rm ext}}\right)dn', \qquad [2]$$

where n is the actual (not volume equivalent) number of condensed solvent molecules present in the particle, n' is a dummy integration variable, and $W(n)$ is the reversible work required to condense n molecules from the surrounding external vapor at pressure $P_{\rm ext}$. The homogeneous nucleation barrier profile is recovered for $n_{\rm seed} = 0$, in which case $n = g$. A derivation of Equation (2) that includes its extension to an arbitrary vapor pressure dependence on particle size is provided in the Supplementary Information, together with a detailed derivation of the various subregion areas, R_i, indicated in Figure 1.

Figure 1 illustrates area constructions for both homogeneous and heterogeneous nucleation using water vapor at 200% relative humidity (RH) as an example. For the homogeneous case, the reduced barrier height is (Supplementary Information):

$$\frac{W_{\rm homo}^{*}}{kT}=R_1+R_2, \qquad [3]$$

which follows from Equation (2) for the upper limit of integration set at $n = n^* = g^*$, the intersection of the Kelvin curve (solid curve) and the horizontal dashed line. In the heterogeneous case, for seed volume $v_{\rm seed}$, the integration in Equation (2) is from $n' = 0$ ($g = v_{\rm seed}/v_1$) to n^* ($g = g^*$), yielding the reduced barrier height (Supplementary Information):

$$\frac{W_{\rm hetero}^{*}}{kT}=R_1. \qquad [4]$$

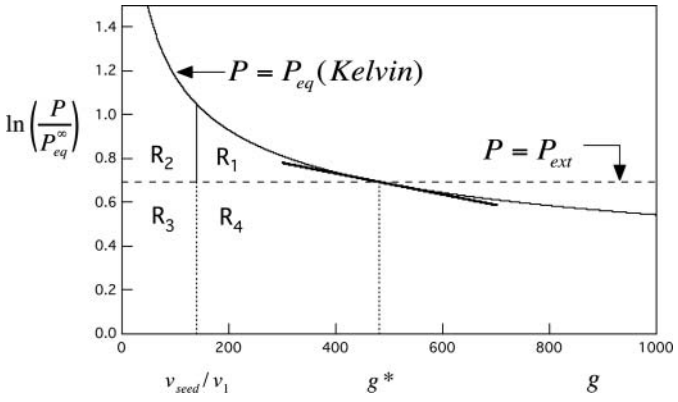

FIG. 1. Area constructions derived from the Kelvin curve. Solid curve is the Kelvin curve for water from Equation (1). Horizontal dashed line is for a water vapor saturation ratio of 2 (relative humidity = 200%). The point of intersection marks the critical drop size, g^*, consisting of the seed particle plus $n^* = g^* - v_{\text{seed}}/v_1$ molecules of condensed water. See text for interpretation of labeled areas $R_1 - R_4$ and the tangent line.

A conceptual advantage of the new approach is that, in principle, it avoids the arbitrary separation into surface and bulk properties inherent in the capillarity drop model. Thus, if the true vapor pressure curve $P_1(n)$, not shown in Figure 1, were somehow available, e.g., from a molecular simulation of cluster evaporation rate, Equation (2) would remain valid—the only requirements being an ideal vapor mixture (an excellent approximation at near-atmospheric pressure conditions) and cluster condensation and evaporation rates that satisfy detailed balance. In the absence of a sufficiently accurate molecular-based approach, we continue with the capillarity approximation, in which case the barriers from graphical construction reduce exactly to those derived conventionally from the classical nucleation theory (Supplementary Information).

Several well-known, capillarity-based relations for the barrier height follow easily from the graphical construction when the vapor pressure is given by the Kelvin relation. Continuing with the homogeneous case, we obtain the following two equivalent results:

$$\frac{W^*_{\text{homo}}}{kT} = \frac{1}{2}g^* \ln\left(\frac{P_{\text{ext}}}{P^{\infty}_{\text{eq}}}\right) = \frac{1}{2}(R_3 + R_4), \qquad [5a]$$

$$\frac{W^*_{\text{homo}}}{kT} = \frac{1}{3}\frac{A^*\sigma}{kT} = \frac{1}{3}(R_1 + R_2 + R_3 + R_4), \qquad [5b]$$

where $A^* \equiv A(g^*)$ is the surface area of the critical cluster (Supplementary Information). Equation (5a) is important to the scaling analysis in Section 5. Unified full barrier profiles for either heterogeneous or homogeneous ($n_{\text{seed}} = 0$) nucleation follow from Equation (2), with limits of integration from n_{seed} to $n_{\text{seed}} + n$ for variable n, where n is the number of molecules of liquid condensate,

$$\frac{W(n)}{kT} = R_1(n) = -n \ln\left(\frac{P_{\text{ext}}}{P^{\infty}_{\text{eq}}}\right) + (36\pi)^{1/3}\left(\frac{\Omega}{T}\right)[(n_{\text{seed}} + n)^{2/3} - n_{\text{seed}}^{2/3}), \qquad [6]$$

in agreement with the classical result. Ω/T is the previously defined physical constant grouping, appearing within parentheses, on the right-hand side of Equation (1). The function $R_1(n)$ evaluated at the critical size $n = n^*$ equals R_1. Dividing the first and second terms on the right-hand side of Equation (6) by the middle terms from Equations (5a) and (5b), respectively, gives the following working-fluid-independent result:

$$\frac{W(n)}{W^*_{\text{homo}}} = 3\left(\frac{n}{g^*} + f\right)^{2/3} - 2\left(\frac{n}{g^*} + f\right) - (3f^{2/3} - 2f), \qquad [7]$$

where $f = v_{\text{seed}}/(g^* v_1) = n_{\text{seed}}/g^*$ is the ratio of seed volume to volume of the critical particle. Equation (7) has been written in expanded form, where $-2f$ and $2f$ are added to the second and the third bracketed term, respectively, to show that at the critical condition, $W(n^*) = W^*$, where $n^*/g^* + f = 1$ and the sum of the two leading terms on the right-hand side is unity,

$$\frac{W^*}{W^*_{\text{homo}}} = \frac{R_1}{R_1 + R_2} = -3f^{2/3} + 2f + 1. \qquad [8]$$

The first equality follows Equations (3) and (4); the "hetero" subscript of Equation (4) having been dropped, noting that homogeneous nucleation is just a special case of the graphical construction with $R_2 = 0$. The homogeneous ($f = 0$) limit of Equation (7) was utilized previously (McGraw 2001). The unified result obtained here shows that the barrier profiles for perfect wetting are characterized by a universal one-parameter family of curves independent of the detailed physiochemical properties of the condensing fluid. These curves are shown for several values of f in Figure 2.

For use in the following section, we require the Zeldovich factor, which is a measure of barrier curvature at the critical size (Abraham 1974):

$$Z = \sqrt{\frac{-1}{2\pi}\left[\frac{\partial^2(W^*_{\text{homo}}/kT)}{\partial g^2}\right]_{g^*}} = \sqrt{\frac{-1}{2\pi}\left[\frac{\partial^2(W^*_{\text{hetero}}/kT)}{\partial n^2}\right]_{n^*}} = \sqrt{\frac{-\gamma}{2\pi}}. \qquad [9]$$

The first equality is the definition of this quantity. The second equality shows that Z has the same value for the homogeneous nucleation and the perfect wetting heterogeneous nucleation cases. This follows by inspection of the graphical construction

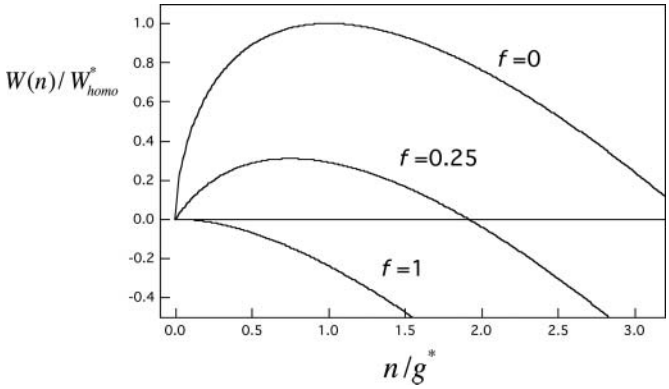

FIG. 2. Scaled nucleation barrier profiles from Equation (7) for several seed volume fractions ($f = n_{\text{seed}}/g^*$). Curves, top to bottom: homogeneous nucleation case ($f = 0$), an intermediate heterogeneous nucleation case ($f = 0.25$), and the Kelvin limit ($f = 1$).

and provides an interpretation for the second partial derivatives as each equals the slope, γ, of the tangent line to the Kelvin curve at g^*, indicated in Figure 1. Mathematically, this result derives from Equation (2): taking the first derivative of this equation with respect to n gives $\ln(P_{\text{eq}}(n)/P_{\text{ext}})$ on the right-hand side, which on differentiation again gives the slope of $\ln P_{\text{eq}}(n)$ at n. Equation (9) results with $n = n^*$ and $g = g^*$. That the same Zeldovich factor applies in the two cases is seen graphically as a simple consequence of the upper limits of integration being located at the same Kelvin size. Vehkamäki et al. (2007) provide a convenient formula for evaluating Z for heterogeneous nucleation on spherical particles under more general nonzero contact angle conditions. Using their results, we have shown (unpublished) that the same area and slope constructions for W^*_{hetero}/kT and Z, respectively, apply as well in the more general case. Of course, $P_{\text{eq}}(n)$ depends on the contact angle and only (discontinuously) reduces to the Kelvin curve for perfect wetting. Evaluating the slope of the Kelvin curve, i.e., the derivative of Equation (1), gives:

$$Z = \sqrt{\frac{1}{6\pi}\frac{\ln S_{\text{ext}}}{g^*}} = \frac{1}{8\pi}\left(\frac{\Omega}{T}\right)^{-3/2}(\ln S_{\text{ext}})^2, \qquad [10]$$

where in the second equality, g^* has been eliminated in favor of $\ln S_{\text{ext}} \equiv \ln(P_{\text{ext}}/P^{\infty}_{\text{eq}})$.

3. MFPT KINETICS AND ACTIVATION RATE

Consider a collection of condensate-free ($n = 0$) seed particles, M, of initial vapor phase concentration $[M]_0 = N(0)$, uniform diameter d_{seed}, and zero contact angle for wetting by the working fluid. The subsequent uptake and exchange of molecules from the working fluid, present in the supersaturated vapor at concentration $[F_1] = n_v$, is described by the following sequence of condensation/evaporation steps:

$$\begin{aligned} M + F_1 &\leftrightarrow MF_1 \\ MF_1 + F_1 &\leftrightarrow MF_2 \\ &\vdots \\ MF_n + F_1 &\leftrightarrow MF_{n+1} \end{aligned} \qquad . \qquad [11]$$

A similar kinetics applies to homogeneous nucleation on replacement of M by F_1. Particles sufficiently large (e.g., twice the critical cluster size MF_{n^*}) are assumed far enough into the growth-dominated regime that they no longer re-cross the barrier at any reasonable rate. This is essentially the same argument used to introduce the Szilard absorbing boundary condition in the classical nucleation theory (Abraham 1974), and for the present application, justifies the placement of an imaginary model boundary distinguishing "un-activated" from "activated" particles. Because the boundary is in effect absorbing (no-returns), the model activation rate equals the rate of its first crossing, or MFPT.

3.1. Model Assumptions

We use an exponential decay model (by Winkler et al. [2008]):

$$\frac{dN}{dt} = -J_{\text{hetero}} = -J_1 N. \qquad [12]$$

In the last equality, particles are treated as independent to the extent that the steady-state nucleation rate, J_{hetero} (number of particles activated per unit volume per second), is proportional to the number concentration of remaining un-activated particles, N:

$$J_{\text{hetero}} = NJ_1, \qquad [13]$$

where J_1 is the per-particle crossing rate. During a short time interval dt, $J_{\text{hetero}}dt$ particles per unit volume are lost to activation. Combining these results gives

$$N(t) = N(0)e^{-J_1 t}, \qquad [14]$$

where $N(0)$ is the initial number concentration of seed particles, and the exponent gives the probability that any given particle remains un-activated at time t. Several assumptions are implicit in the model that a direct calculation of the MFPT and comparison with measurement can test. First, the assumption of steady-state nucleation rate: conditions under which the quasi-equilibration of precritical clusters and steady-state nucleation are reached on time scales shorter as compared with the decay of N can be seen from a calculation of the MFPT as a function of the absorbing boundary location, as described in connection with Figure 3. Second, the exponential decay model requires random rather than deterministic activation—a property that can also be

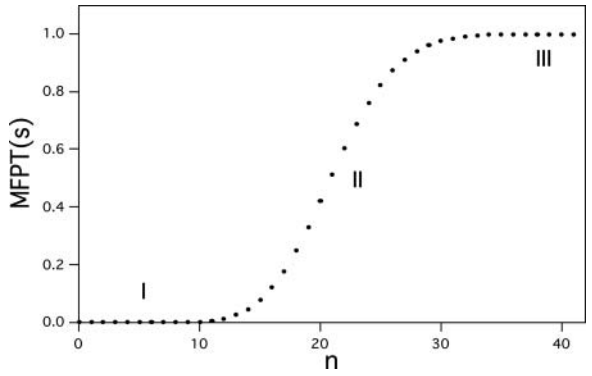

FIG. 3. Typical behavior of the mean first passage time (MFPT) to reach a given cluster size as a function of that size. Here, n is the number of molecules condensed onto the seed. Region I, quasi-equilibrium between clusters of precritical size. Region II, inflection point at the critical size. Region III, rapid-growth regime. Calculations are for heterogeneous nucleation of *l*-menthol on a 1.5-nm-diameter seed. $S_{\text{ext}} = 86.0$, $W^*/kT = 18.1$, $J_1 = 1\ \text{s}^{-1}$.

checked through a study of the MFPT. Finally, Equation (12) assumes that just one seed particle is present in the critical nucleus. This is easily tested experimentally using the nucleation theorem (Equation (24)) below.

3.2. Calculation of the MFPT

We classify un-activated (activated) particles as those belonging to size class $MF_{n\text{max}}$ and smaller ($MF_{n\text{max}+1}$ and larger), where $n\text{max} = 2n^*$. Our interest is primarily in the MFPT to reach $MF_{n\text{max}+1}$ so defined, but a study for variable $n$max, to show insensitivity to boundary placement at $2n^*$ and verify other assumptions implicit in the exponential model, was also carried out. Let U be the domain of un-activated particles such that $MF_n \in U$ for $0 \le n \le n\text{max}$, and let $P_U(t)$ be the probability that a seed that is condensate-free at $t = 0$ remains in the un-activated domain at time t. Then, the fraction of particles *leaving* U at time t is $-dP_U(t)/dt$. By definition, the MFPT is the mean time it takes to leave U, which is (Hänggi et al. 1990):

$$\tau \equiv -\int_0^\infty t\frac{dP_U}{dt}dt = \int_0^\infty P_U(t)dt. \qquad [15]$$

The last equality follows an integration by parts. Evaluating the last integral using $P_U(t) = N(t)/N(0) = \exp(-J_1 t)$ from Equation (14) for the exponential decay model gives $\tau = 1/J_1$, showing that the MFPT equals the reciprocal of the per-particle crossing rate.

Benchmark calculations are based on the following formula for the MFPT (Hänggi et al. 1990; Wedekind et al. 2007):

$$\tau(n\text{max}) = \sum_{j=0}^{n\text{max}}\left(\frac{e^{W_{\text{hetero}}(j)/kT}}{D_j}\sum_{i=0}^{j}e^{-W_{\text{hetero}}(i)/kT}\right). \qquad [16]$$

The double summation is a discretized version of Equation (2) of Wedekind et al. (2007). Dummy indices i and j refer to the number of condensate molecules in the seed-condensate particle (the n in MF_n) and the summation begins with the initial seed, M ($n = 0$). Equation (16) describes the case of particles undergoing diffusion and drift, along the size coordinate, n, with reflecting and absorbing boundaries located at 0 and $n\text{max} + 1$, respectively. D_j is the size-dependent diffusion coefficient along the size coordinate, which is also equal to the collision rate of vapor molecules, with a particle of size $n = j$ ($g = n_{\text{seed}} + j$) (McGraw 2001):

$$D_j = n_v\sqrt{\frac{8\pi kT}{m_v}}r_1^2(n_{\text{seed}} + j)^{2/3} = \frac{P_{\text{ext}}A(j)}{\sqrt{2\pi m_v kT}}. \qquad [17]$$

Here, r_1 is the vapor monomer radius corresponding to the molecular volume v_1, n_v is the vapor number concentration, m_v is vapor molecular mass, and $A(j) = 4\pi r_1^2(n_{\text{seed}} + j)^{2/3}$ is the surface area of the seed–condensate cluster for $n = j$. Direct evaluation of the double summation of Equation (16) provides the benchmark against which a new approximate formulation for J_1 will be tested and used to analyze the scaling properties of heterogeneous particle activation rate in the following section.

4. A SIMPLE BUT ACCURATE EXPRESSION FOR MFPT AND HETEROGENEOUS NUCLEATION RATE

Figure 3 illustrates a typical distribution of the MFPTs required to exceed any specified (seed plus condensate) particle size as a function of that size or, equivalently, as a function of the upper limit, $n$max, in the double summation of Equation (16). The steep inflection region centered at the critical size (region II) is indicative of a wide separation of time scales between the rapid quasi-equilibration of precritical particles (region I) and the significantly longer times required for barrier crossing and depletion of N, which occur on the order of $\tau = 1/J_1$. The figure also shows the MFPT to be insensitive to $n$max sufficiently beyond the critical particle size (region III). Henceforth, we set $n\text{max} = 2n^*$. Starting with Equation (16), a simple but accurate expression can be derived for the MFPT and the per-particle heterogeneous nucleation rate. The result, with details of the derivation provided in the Supplementary Information, is:

$$J_1 = \frac{1}{\tau} \approx \frac{P_{\text{ext}}A(j^*)}{\sqrt{2\pi m_v kT}}(1 - e^{-h})Ze^{-W^*_{\text{hetero}}/kT}. \qquad [18]$$

Multiplication by N gives the total heterogeneous nucleation rate:

$$J_{\text{hetero}} \approx N\frac{P_{\text{ext}}A(j^*)}{\sqrt{2\pi m_v kT}}(1 - e^{-h})Ze^{-W^*_{\text{hetero}}/kT}. \qquad [19]$$

The reaction set defined by Equation (11) describes an associating vapor and a correction for association is included in the rate through the factor $(1 - e^{-h})$, where h is the length

of the vertical line segment separating regions R_1 and R_2 in Figure 1 (see Supplementary Information). In the limit of large h, the distribution of precritical seed–condensate clusters is dominated by the $n = 0$ condensate-free seeds, M, and $[M] = N$. For the general case that association is present, $[M] = (1 - e^{-h})N$ and Equation (19) becomes

$$J_{\text{hetero}} \approx [M] \frac{P_{\text{ext}} A(j^*)}{\sqrt{2\pi m_v kT}} Z e^{-W^*_{\text{hetero}}/kT}, \qquad [20]$$

which is proportional to the concentration of the starting species—seeds without condensate. The concentration of condensate-free seeds $[M]$, treated here as just another molecular constituent of the vapor, is reduced below N by the association factor $1-e^{-h}$, and J_{hetero} is correspondingly reduced. This is an example of the somewhat counterintuitive effect that association has on increasing the stability of a metastable vapor phase through suppression of the nucleation rate (Katz et al. 1966).

4.1. Homogeneous Nucleation Rate

At high-enough saturation ratio, homogeneous nucleation of the vapor itself will compete with heterogeneous nucleation and interfere with particle detection, making the comparison of these two nucleation channels a necessary consideration. The homogeneous nucleation rate is (Abraham 1974)

$$\begin{aligned} J_{\text{homo}} &= n_v \left(\frac{P^{\infty}_{\text{eq}}}{P_{\text{ext}}} \right) \frac{P_{\text{ext}} A(g^*)}{\sqrt{2\pi m_v kT}} Z e^{-W^*_{\text{homo}}/kT} \\ &= n^{\text{eq}}_v \frac{P_{\text{ext}} A(g^*)}{\sqrt{2\pi m_v kT}} Z e^{-W^*_{\text{homo}}/kT}. \end{aligned} \qquad [21]$$

As noted previously, Z has the same value here as in the heterogeneous case. The vapor pressure ratio, within parentheses to the right of the first equality, supplies the $1/S_{\text{ext}}$ correction due to Courtney (1961). It should be noted that Courtney's correction, which derives from the addition of a term $kT \ln(P_{\text{ext}}/P^{\infty}_{\text{eq}})$ to the classical W_{homo} in order to gain consistency with the law of mass action, does not apply to W_{hetero} because the correction cancels on taking free-energy differences relative to M when a seed is present.

4.2. Testing the New Rate Expression

Figures 4 and 5 show the Kelvin curve, together with the calculated homogeneous nucleation threshold range from Equation (21) (here shown for rates within ±2 orders of magnitude of $J_{\text{homo}} = 1$ cm^{-3}s^{-1}) and heterogeneous nucleation threshold range from Equation (18) (rates within ±2 orders of magnitude of $J_{\text{hetero}} = 1$ cm^{-3}s^{-1}, which numerically equals J_1(s^{-1}) for $N = 1$ cm^{-3}). The filled circles are from the full double summation for the MFPT for $\tau = 1$ s (Equation (16) with $n\max = 2n^*$) and should be compared with the approximate expression (middle curve) for $J_{\text{hetero}} = 1$. Agreement is excellent: to within about 5% in the case of menthol and 2% for water. The larger discrepancy for menthol is probably due to discretization error as the number of molecules in the critical nucleus is considerably less in the case of methanol than the case of water. Barrier heights where the unity nucleation rate thresholds intersect are 18.5 kT for menthol (Figure 4) and 18.3 kT for water (Figure 5), i.e., much lower than for homogeneous nucleation, where typical barrier heights range between 50 and 70 kT (see Equation (26) below and parameters given in Table 1 for calculation of the heterogeneous barrier height). Closer to the region where the seed diameter approaches the Kelvin diameter, e.g., for barrier heights lower than about 5 kT, the approximations used to derive the new analytic expression begin to fail and so the full double-summation formula for the MFPT should

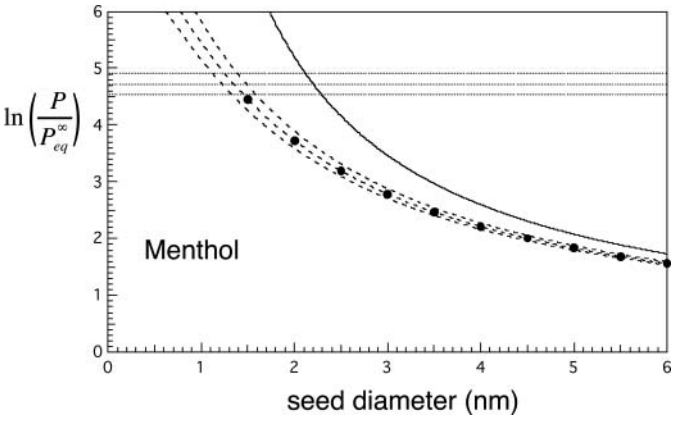

FIG. 4. Nucleation rates for menthol. Solid curve is the Kelvin limit. Dashed lines and curves are contours of constant nucleation rate. Horizontal lines: contours of constant homogeneous nucleation rate: top to bottom, $J_{\text{homo}} = 100$, 1, and 0.01 cm^{-3}s^{-1}. Dashed curves give similar contours for the heterogeneous nucleation rate from the new approximate prefactor-exponent form: top to bottom, $J_{\text{hetero}} = 100$, 1, and 0.01 cm^{-3}s^{-1} for $N = 1$ cm^{-3}. Markers: results from the double-summation calculation for mean first passage time, $J_1 = 1$ cm^{-3}s^{-1}. These show excellent agreement with the approximate result (middle curve).

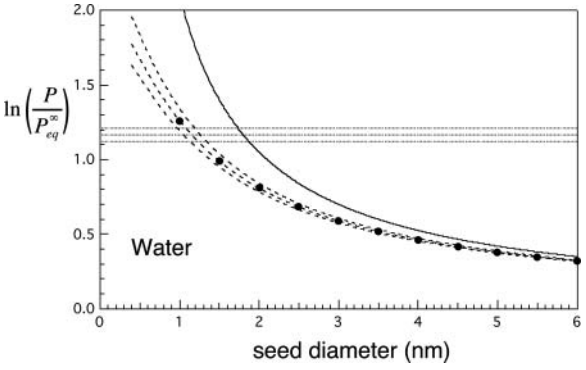

FIG. 5. Nucleation rates for water. Solid curve is the Kelvin limit. Dashed lines and curves are contours of constant nucleation rate. Horizontal lines: contours of constant homogeneous nucleation rate: top to bottom, $J_{\text{homo}} = 100$, 1, and 0.01 cm^{-3}s^{-1}. Dashed curves give similar contours for the heterogeneous nucleation rate from the new approximate prefactor-exponent form: top to bottom, $J_{\text{hetero}} = 100$, 1, and 0.01 cm^{-3}s^{-1} for $N = 1$ cm^{-3}. Markers: results from the double-summation calculation for mean first passage time, $J_1 = 1$ s^{-1}. These show excellent agreement with the approximate result (middle curve).

TABLE 1

Parameters and scaling properties for the four working fluids included in Figure 7 and the theoretical minimum particle size ($d_{\text{seed}}^{\min}$) that can be detected by each for $N = 1$ cm^{-3} at the threshold conditions $J_{\text{homo}} = J_{\text{hetero}} = 1$. Other properties include the critical saturation ratio for homogeneous nucleation, S_{cr}; dimensionless corresponding states parameter, Ω/T; log vapor saturation ratio in unstable equilibrium with the minimum detectable particle size, h; molecular number concentration of vapor in equilibrium with bulk liquid, n_v^{eq}; and the volume per molecule of bulk liquid working fluid, v_1. Note comparative constancies of homogeneous nucleation barrier height and $f^{\min} = n_{\text{seed}}^{\min}/g^*$. Data sources: *l*-menthol, Becker and Reiss (1978); *n*-nonane, Rudek et al. (1996); *n*-butanol, Magnusson et al. (2003); water: Wölk and Strey (2001)

Property	*l*-Menthol	*n*-Nonane	*n*-Butanol	Water
S_{cr}	111.5	7.41	3.11	3.20
T (K)	323.15	300.00	300.00	298.15
Ω/T	4.19	2.40	1.64	1.69
g^*	23.6	57.8	101.6	102.2
W_{homo}^*/kT	55.5	57.9	57.7	59.5
$n_v^{\text{eq}}(\text{cm}^{-3})$	1.19×10^{16}	1.57×10^{17}	2.58×10^{17}	7.69×10^{17}
$f^{\min}(N = 1)$	0.230	0.244	0.254	0.251
$h(f^{\min})$	2.98	1.20	0.66	0.68
$n_{\text{seed}}^{\min}$	5.4	14.1	25.8	25.7
$v_1(\text{cm}^3)$	2.38×10^{-22}	2.99×10^{-22}	1.53×10^{-22}	3.00×10^{-23}
$d_{\text{seed}}^{\min}(\text{nm})$	1.35	2.00	1.96	1.14

be used instead. The exponential decay model (Equation (14)) will also fail in this regime as activation begins to take on less the character of a random barrier crossing process and more of deterministic growth. According to the 5 kT criterion, the simplified expression for heterogeneous nucleation rate can be used reliably for $f \leq 0.5$ (or $d_{\text{seed}}/d_{\text{Kelvin}}$ less than about 80%). This is the predominant range of interest anyway as the general goal is to achieve selective detection of the smallest particles, which is favored by being close to the heterogeneous nucleation threshold and well below the Kelvin limit. For $f \leq 0.5$, the association factor is typically between 0.2 and 1, while $1/S_{\text{ext}}$ typically exceeds 0.01. In the context of nucleation, such corrections are often regarded as small, but here, they are needed to achieve the few percentage level of accuracy with reference to the MFPT benchmark we have described.

4.3. Nucleation Theorems

Nucleation theorems give the relative sensitivity of nucleation rate to saturation ratio, temperature, or other constraints (Kashchiev 1982; McGraw and Wu 2003; Vehkamäki et al. 2007). The following relations in terms of the log saturation ratio follow immediately from the area construction (Figure 1) on application of the fundamental theorem of integral calculus to the areas R_1 and $R_1 + R_2$:

$$\frac{\partial \ln J_{\text{hetero}}}{\partial \ln S_{\text{ext}}} = \frac{\partial \ln K_{\text{hetero}}}{\partial \ln S_{\text{ext}}} - \frac{\partial W_{\text{hetero}}^*/kT}{\partial \ln S_{\text{ext}}} = 1 - \frac{\partial(R_1)}{\partial \ln S_{\text{ext}}} = 1 + g^* - n_{\text{seed}} = 1 + n^*, \quad [22]$$

$$\frac{\partial \ln J_{\text{homo}}}{\partial \ln S_{\text{ext}}} = \frac{\partial \ln K_{\text{homo}}}{\partial \ln S_{\text{ext}}} - \frac{\partial W_{\text{homo}}^*/kT}{\partial \ln S_{\text{ext}}} = 1 - \frac{\partial(R_1 + R_2)}{\partial \ln S_{\text{ext}}} = 1 + g^*. \quad [23]$$

Partial derivatives are taken at constant temperature, and K_{hetero} and K_{homo} are the prefactors from Equations (19) and (21), respectively, for the heterogeneous and homogeneous nucleation rate, each of which makes a contribution of unity to the relative sensitivity. Evaluating instead the relative sensitivity with respect to seed concentration gives

$$\frac{\partial \ln J_{\text{hetero}}}{\partial \ln N} = 1, \quad [24]$$

as expected from the one-seed-per-critical-nucleus assumption. More generally, measurement of $\partial \ln J_{\text{hetero}}/\partial \ln N$ yields the number of seed particles present in the critical nucleus. Another heterogeneous nucleation theorem that follows immediately from inspection of the area construction gives sensitivity of the log rate to changes in seed particle size, n_{seed}:

$$\frac{\partial \ln J_{\text{hetero}}}{\partial n_{\text{seed}}} \approx -\frac{\partial R_1}{\partial n_{\text{seed}}} = h \ (h \geq 0). \quad [25]$$

The approximate equality neglects a small contribution from the association term in the kinetic prefactor. The requirement that h be nonnegative is discussed in Section 6.

5. FUNDAMENTAL LIMITS TO NEUTRAL PARTICLE DETECTION

5.1. Maximizing Detector Sensitivity

Avoiding interference from homogeneous nucleation requires that the homogeneous nucleation rate be less than or comparable to the activation rate: $J_{\text{homo}}/J_{\text{hetero}} \leq 1$ or, from Equation (13), $J_{\text{homo}}/J_1 \leq N$ (cm^{-3}). Under typical CPC measuring conditions, N is in the 10–1000 cm^{-3}range. Nucleation thresholds are typically sharp, as illustrated for menthol and water in Figures 4 and 5, respectively, for $N = 1$ cm^{-3}. The figures show threshold bands, where the rates J_{homo} and J_{hetero} take on middle and extreme values of 1, 10^{-2}, and 10^{2}, and characteristically small intersection regions, where the ratio $J_{\text{homo}}/J_{\text{hetero}}$ ranges from 10^{-4} to 10^{4}. Operating a CPC just below the homogeneous nucleation threshold, $J_{\text{homo}} = 1$ $\text{cm}^{-3}\text{s}^{-1}$, which defines the critical saturation ratio S_{cr}, avoids interference from homogeneous nucleation, while maximizing sensitivity for smallest particle detection. The smallest particles will be detected under conditions that are simultaneously close to the homogeneous and heterogeneous nucleation thresholds, while preserving the above inequalities. These conditions are used next to establish fundamental size and concentration limits to neutral particle detection.

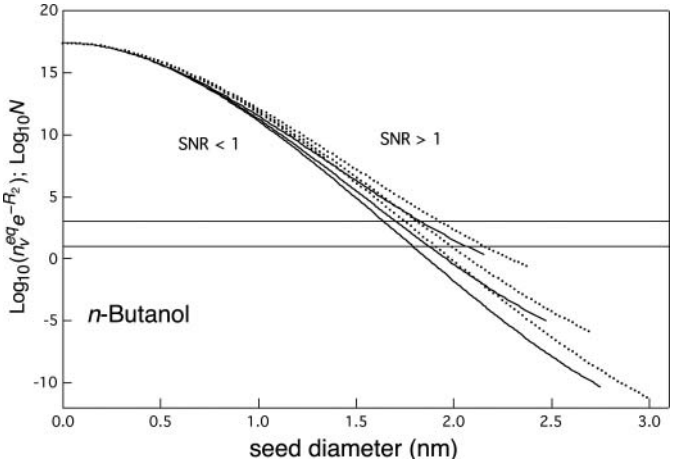

FIG. 6. Curves of equal heterogeneous and homogeneous nucleation rates (SNR = 1) for n-butanol. Logarithm of $n_v^{\text{eq}}e^{-R_2}$ or N (these quantities are equal along these curves from Equation (26)) versus seed diameter (nm). Solid curves: $T = 300$ K, top to bottom, $J = 10^6(S_{\text{ext}} = 3.67)$, $J = 1(S_{\text{ext}} = 3.11)$, $J = 10^{-6}(S_{\text{ext}} = 2.78)$. Dashed curves: $T = 320$ K, top to bottom, $J = 10^6(S_{\text{ext}} = 2.87)$, $J = 1(S_{\text{ext}} = 2.56)$, $J = 10^{-6}(S_{\text{ext}} = 2.31)$. Results are shown for $d_{\text{seed}}/d_{\text{Kelvin}} < 0.8$, beyond which the barrier height is lower than 5 kT. Signal-to-noise ratios for a given set of conditions exceed (are less than) unity to the right of and above (left and below) the corresponding curve. Horizontal lines: typical range for N in CPC measurements (10^1–10^3 cm^{-3}).

5.2. Signal-to-Noise Ratio Perspective

Taking nucleation rates from Equations (19) and (21), the preceding criterion becomes

$$\begin{aligned}\frac{J_{\text{homo}}}{J_{\text{hetero}}} &= \frac{n_v^{\text{eq}}}{N}\left(\frac{1}{1-e^{-h}}\right)\frac{A(g^*)}{A(n^*)}e^{-(W^*_{\text{homo}}-W^*_{\text{hetero}})/kT} \\ &= \frac{n_v^{\text{eq}}}{N}\left\{\left(\frac{1}{1-e^{-h}}\right)e^{-R_2}\right\} \approx \frac{n_v^{\text{eq}}}{N}e^{-R_2} \\ &= \frac{n_v^{\text{eq}}}{N}\exp\left[-\frac{W^*_{\text{homo}}}{kT}\left(3f^{2/3}-2f\right)\right] \leq 1. \qquad [26]\end{aligned}$$

The second equality uses the fact that the surface area ratio is unity. As before, $f = n_{\text{seed}}/g^*$ and R_2, the area under the Kelvin curve referenced in Figure 1, has been evaluated in the last equality using Equation (8). In the approximate equality, we neglect the inverse association factor, which as noted previously is typically close to unity and much less important to the subsequent discussion than n_v^{eq}, R_2, or N. The expression to the right of the approximate equality has an especially transparent interpretation in terms of the signal-to-noise ratio: For steady-state homogeneous nucleation, the constrained equilibrium concentration of clusters of size n_{seed} is given by $n_v^{\text{eq}}e^{-R_2}$, where R_2 is the reversible work required to assemble a precritical cluster of this size from vapor in the capillary drop model. (That the concentration of vapor in equilibrium with bulk liquid n_v^{eq} appears, rather than the actual supersaturated vapor concentration n_v, follows Courtney [1961].) Although these precritical clusters arise from thermal fluctuations in the vapor, they have the same probability to subsequently grow to critical size and contribute to homogeneous nucleation rate that the permanent perfect wetting seeds have of contributing to the heterogeneous nucleation rate. Whenever the two concentrations are equal, the homogeneous and heterogeneous nucleation rates will also be the same. The expression to the right of the approximate equality is simply this ratio of concentrations: fluctuating clusters of seed size (thermal noise) to actual seeds N (signal). Viewed from this perspective, the ratio $n_v^{\text{eq}}e^{-R_2}/N$, like its equivalent $J_{\text{homo}}/J_{\text{hetero}}$, should normally be maintained less than unity, and its inverse, the signal-to-noise ratio (SNR), greater than unity in order that the concentration of homogeneously formed clusters not exceed the concentration of seeds. (One can conceive of tricks to work with lower SNRs, such as modulating the seed concentration, but such considerations are beyond the scope of the present study.) Figure 6 shows curves of constant SNR = 1 (equivalently, curves for which $N = n_v^{\text{eq}}e^{-R_2}$) for n-butanol at two different temperatures and three different nucleation rates obtained by varying S_{ext}. Detection at smaller size is seen to be favored by higher N, lower T, and lower S_{ext} for a relatively lower homogeneous nucleation rate.

5.3. Scaling and Minimum Detection Size

Because the working fluid enters primarily through its equilibrium vapor pressure and nondimensional *homogeneous* nucleation parameters, corresponding states scaling ideas previously developed to correlate the homogeneous nucleation thresholds of supersaturated vapors (McGraw 1981; Rasmussen and Babu 1984; Hale 1992) can be used here. The power of

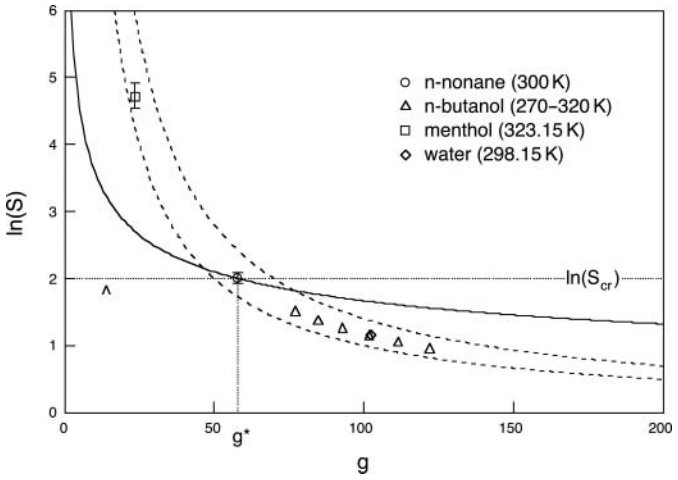

FIG. 7. Scaled nucleation rate. Dashed hyperbolic curves: contours of constant homogeneous nucleation barrier height, 50 kT (lower curve) and 70 kT (upper curve). The region between these curves provides a good indication of homogeneous nucleation threshold range for most substances. Markers show four candidate working fluids and are centered on the critical cluster size and critical saturation ratio (as indicated here for the case of nonane), which for each fluid gives $J_{\text{homo}} = 1\ \text{cm}^{-3}\text{s}^{-1}$. Error bars show a four order of magnitude range in nucleation rate from $J_{\text{homo}} = 0.01\ \text{cm}^{-3}\text{s}^{-1}$ to $J_{\text{homo}} = 100\ \text{cm}^{-3}\text{s}^{-1}$. No error bar means that the height of the symbol itself exceeds this range. The solid curve is the Kelvin curve for nonane ($\Omega/T = 2.40$ at $T = 300$ K). The horizontal and vertical dotted lines for nonane mark the logarithm of its critical saturation ratio $\ln(S_{\text{cr}})$ and g^*, respectively. The area of the rectangle bounded by these lines and the axes is twice the reduced barrier height, W^*_{homo}/kT. The caret marks the $N = 1\ \text{cm}^{-3}$ detection limit for nonane.

scaling is illustrated through its application to a selection of four widely different working fluids for which homogeneous nucleation measurements are available (Figure 7; Table 1). Homogeneous nucleation barrier heights for many substances tend to be in the $50-70\ kT$ range bounded by the dashed hyperbolic curves (McGraw 1981), as illustrated for these four fluids in Figure 7. Each of the fluid-characteristic points shown in the figure lies at the intersection of several important curves. To avoid crowding the figure, these are drawn only for nonane to illustrate the method. They include the curve of constant homogeneous nucleation barrier height (Equation (5a), which if drawn would pass through the nonane point and lie within the hyperbolic dashed curves), the Kelvin curve (which depends on the scaling parameter Ω/T), and the horizontal and vertical lines marking $\ln S_{\text{cr}}$ and g^*, respectively. The parameters needed to construct similar sets of curves for each of the other working fluids are provided in the table.

The maximum sensitivity condition for each working fluid lies close to the critical saturation ratio, indicated in Figure 7 for nonane by the horizontal dotted line. The threshold values in the first row of Table 1 were obtained from Equation (21) by adjusting S_{ext} to have $J_{\text{homo}} = 1$. Thus, the minimum detectable size lies close to the $\ln(S_{\text{cr}})$ line, between 0 and g^*, and close to the heterogeneous nucleation threshold. Its precise location is obtained by solving Equation (26) (here with seed concentration $N = 1\ \text{cm}^{-3}$) for the equality condition $J_{\text{homo}}/J_{\text{hetero}} = 1$. The result, with $n^{\min}_{\text{seed}} \equiv f^{\min} g^*$, is marked by the caret in Figure 7 for nonane and provided for the other fluids in row 9 of Table 1. Near constancy of $f^{\min}$ (row 7) for the different working fluids suggests its value as an important *heterogeneous* nucleation scaling parameter. Using molecular volumes, obtained from the bulk liquid density (row 10), to convert $n^{\min}_{\text{seed}}$ to a spherical mass-equivalent volume gives the minimum detectable seed particle diameters shown in the last row of the table. The entries for menthol and water match particle diameters at the intersection of the threshold rates, $J_{\text{homo}} = J_{\text{hetero}} = 1$, shown in Figures 4 and 5, respectively. The smallest diameter, at 1.14 nm, is found for water even though its scaling parameters are very close to those of *n*-butanol at 300 K, which has the second highest minimum detection diameter, 1.96 nm. The $n^{\min}_{\text{seed}}$ values are close for water and *n*-butanol, so the difference lies predominately in the smaller molecular volume for water. Comparing water and menthol, we observe that the latter has the highest Ω/T (row 3), which gives it the smallest g^* (row 4). Here again, water wins out for having the smaller detection diameter due to its factor-of-eight smaller molecular volume.

The scaling parameter Ω/T contains T implicitly in Ω and explicitly in $1/T$. A useful approximate form for the temperature dependence of Ω/T has been obtained by Hale (1992) for surface tensions approximated by a linear form, $\sigma = \sigma_0(T_c - T)$, where T_c is the critical temperature. Neglecting a small temperature dependence in density gives $\Omega/T \approx \Omega_{\text{H}}(T_c/T - 1)$, with $\Omega_{\text{H}} \equiv \sigma_0 v_1^{2/3}/k$. Temperature dependence is exhibited in Figure 7 for the case of *n*-butanol at 10° intervals, from 270 to 320 K, by the triangles positioned from left to right, respectively.

5.4. Nucleation and Growth as a Detection Tool

The preceding discussion examined the case that $N \approx 1\ \text{cm}^{-3}$ and applies to the detection of seed particles (or large molecular impurities) of volume $n^{\min}_{\text{seed}} v_1$ present in the vapor at concentrations of order $1\ \text{cm}^{-3}$. The question naturally arises as to whether or not it is possible to detect still smaller particles and even single neutral molecules this way. According to Equation (26) and Figure 6, the detection of molecule "impurities" comparable in size to the molecular volume of the working fluid requires their presence at the much higher concentration $N \approx n_v^{\text{eq}}$. Intermediate sizes require intermediate seed concentrations N (Figure 6). The efficiency of particle detection, equal to activation probability within the CPC, is defined as:

$$\varepsilon = 1 - \frac{N(\tau)}{N(0)} = 1 - e^{-J_1\tau}, \qquad [27]$$

where $N(\tau)$ is the concentration of un-activated particles leaving the CPC after residence time τ. A typical CPC residence time of $\tau = 0.1$ s, and $J_1 = 1\ \text{cm}^{-3}\text{s}^{-1}$, gives $\varepsilon \approx 0.1$, which for this residence time is the detection efficiency at the minimum detectable particle sizes reported in Table 1. Efficiency, being dependent only on the product $J_1\tau$, is a metric that does

not include noise from interfering homogeneous nucleation. On the other hand, from Equation (26), SNR $\approx J_{\text{hetero}}/J_{\text{homo}} = NJ_1/J_{\text{homo}} \approx N\varepsilon/(J_{\text{homo}}\tau)$ includes the homogeneous nucleation effect. The last approximation (from Equation (27)) is useful in the limit of low activation probability. Indeed, ε varies widely along the SNR = 1 curves of Figure 6. Thus, having $N = 100$ cm^{-3} gives a noticeably smaller detectable size than having $N = 1$ at the same SNR. These smaller particles will be detectable at the same rate but at only 1% efficiency relative to the (somewhat larger) detectable size limits reported in Table 1, based on having $N = 1$ cm^{-3}.

Evidence for the detection of critical nuclei containing just one organic molecule comes from laboratory measurements on the ternary p-toluic acid/sulfuric acid/water (Zhang et al. 2004) and cis-pinonic acid/sulfuric acid/water (Zhang et al. 2009) systems and their interpretation using the nucleation theorem (McGraw and Zhang 2008). In both cases, the concentration of the organic acid present in the vapor was of the order 10^{10}cm^{-3}—far in excess of unity, and comparable to the sulfuric acid vapor concentration. For a nucleation rate of 10^3cm^{-3}s^{-1}, this implies detection efficiency for the organic acid in the 10^{-8} range. Noise arises due to binary homogeneous nucleation in the background sulfuric acid/water vapor mixture. Analysis of ternary-to-binary nucleation rate ratios in the *p*-toluic acid/sulfuric acid/water system (Figure 4 of McGraw and Zhang 2008) gives SNRs for detection of *p*-toluic acid in the 5–10 range.

In their investigations of nucleation and growth as a detection tool, Reiss et al. (1977) concluded: "It is unlikely, however, that single neutral molecules can be detected [referring to detection using a diffusion cloud chamber], although the possibility remains for detecting individual polymer molecules of a substantial degree of polymerization" (p. 140). Elsewhere in their paper, on page 29, the authors state: "Even though theory shows that one cannot *detect* a single impurity molecule, it shows that there may be cases in which a nucleus contains only a single [such] molecule. But this is not the same as having *every* impurity molecule serve as a nucleus." Their findings are consistent with the results obtained here. The following section presents a preliminary analysis showing that the graphical method can be used to incorporate departures from the Kelvin relation due to interactions at the molecular scale.

6. INCORPORATING DEPARTURE FROM THE KELVIN RELATION

An important tool for direct testing of the Kelvin relation for small droplets became available with the ability to measure nucleation rates (as opposed to earlier measurements that yielded only nucleation threshold conditions). Strey et al. (1994) performed such a test using homogeneous nucleation rate measurements in conjunction with the nucleation theorem to give a determination of the critical cluster size for *n*-butanol. The Kelvin relation sufficed to predict cluster sizes down to as few as 40 molecules, an equivalent radius of curvature of 1 nm.

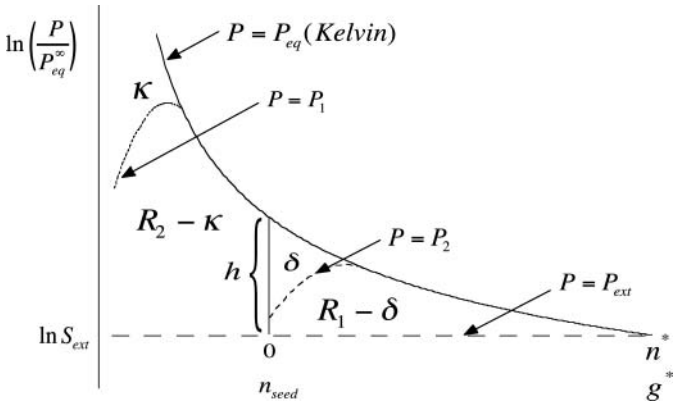

FIG. 8. Area construction similar to Figure 1 but illustrating the effect of interactions that lower the equilibrium vapor pressure relative to the Kelvin curve (solid curve). The dotted curve, which only departs from Kelvin at the smallest cluster sizes, results in a lowering of the barrier height for homogeneous nucleation to $R_1+R_2-\kappa$. The dashed curve shows lowering of the heterogeneous barrier from R_1 to $R_1 - \delta$. Here, h is the length of the vertical line segment (Equation (S18)). Note that the abscissa (upper scale) has been shifted in the heterogeneous case to tally only the number of molecules of condensed working fluid. The lower scale, which runs out to g^*, applies to the homogeneous case.

Similar studies for water showed agreement down to about 30 molecules or about 0.6-nm radius of curvature (Wölk and Strey 2001). One concludes from these studies that even though the Kelvin relation relies on macroscopic surface tension and density to predict the vapor pressures of small drops, it tends to work surprisingly well.

A seemingly common case in homogeneous nucleation occurs when the Kelvin relation works well for clusters of critical size but fails for smaller ones. This situation is depicted schematically in Figure 8 by the dotted vapor pressure curve $[P = P_1(g)]$ for the case of attractive interactions that lower the vapor pressures of very small clusters relative to the Kelvin curve. The integrated area between $P_1(g)$ and the dashed line at $\ln S_{\text{ext}}$ equals the corrected reduced barrier height for homogeneous nucleation, which in this case is *lower* by κ from the prediction of the classical nucleation theory (CNT) based on the Kelvin curve:

$$\kappa = \int_0^{g*} \ln[P_{\text{eq}}(g)/P_1(g)]dg. \qquad [28]$$

In spite of this barrier lowering, g^* and barrier curvature near g^* are the same as in the classical nucleation theory because the location and slope at the crossing point of P_1 and P_{eq} with $\ln S_{\text{ext}}$ remain the same. Thus, the effect of κ is to cause a uniform vertical shift in the barrier relative to CNT, resulting in either a lower (the case depicted here for $\kappa > 0$) or higher ($\kappa < 0$) barrier height: $W^*_{\text{homo}} - W^*_{\text{homo}}(\text{CNT}) = -\kappa kT$. The experimental signature of this effect, in accord with the nucleation theorem, is a vertical shift (also by κ) in curves of $\ln J_{\text{homo}}$ versus $\ln S_{\text{ext}}$, as is commonly seen in rate measurements (Strey et al. 1994; Wölk and Strey 2001). This effect has been studied using

molecular-based theory (McGraw and Laaksonen 1996), but the present graphical approach makes it more transparent. For the case of *n*-butanol, the experimental rate exceeds the classical nucleation theory prediction by about a factor of 10 (Strey et al. 1994), yielding $\kappa \approx 2 - 3$. For water, the observed shifts (and corresponding values of κ) are smaller and undergo a change in sign at about 240 K (Wölk and Strey 2001).

6.1. Substrate–Working Fluid Interactions

Molecular-scale interactions between a particle surface and the working fluid can also result in departure from the Kelvin relation. Such interactions are not easily incorporated into macroscopic properties such as the contact angles and line tensions used by the classical nucleation theory. Evidence for strong surface effects that seem to defy a classical description is seen in recent measurements comparing nanometer-sized particles of Ag and NaCl. These substances show very different activation efficiencies and, in the case of NaCl, unusual temperature dependence (Schobesberger et al. 2010). While not complete without a detailed picture of the interactions in question, the graphical method provides a molecular framework for generalization of the classical nucleation theory based on deviations in vapor pressure (positive or negative) relative to the Kelvin curve. Figure 8 illustrates the case that departures from the classical homogeneous nucleation theory are due to interactions that take place within clusters of the pure working fluid that are smaller than the seed so that $P_1(g) \approx P_{\text{eq}}(g)$ for $g \geq n_{\text{seed}}$, but interactions between the seed and the working fluid can still cause departure from the classical heterogeneous nucleation theory for perfect wetting. The effect on vapor pressure is depicted by the dashed curve $[P = P_2(g)]$ in Figure 8 for the case of attractive interactions, resulting in a vapor pressure lowering near the seed surface. Reduction in *h*, as suggested in the figure, might possibly be inferred through measurements of the relative sensitivity of heterogeneous nucleation rate to seed size using the nucleation theorem of Equation (25). Note, however, that whenever the vapor pressure at n_{seed} falls below P_{ext}, *h* becomes negative. Familiar examples occur in the Thompson theory, for charged particles, and in the Kohler theory for soluble nuclei. In such cases, Equation (25) predicts a relative sensitivity of zero as the particle undergoes spontaneous growth until achieving stable equilibrium at P_{ext}. Considering only positive *h*, the integrated effect of vapor-pressure-lowering interactions is to cause a shift in the heterogeneous nucleation barrier height: $W^*_{\text{hetero}} - W^*_{\text{hetero}}(\text{CNT}) = -\delta kT$, where CNT, within parentheses, refers not only to the classical nucleation theory but also to perfect wetting. δ is the area indicated in Figure 8:

$$\delta = \int_{g=n_{\text{seed}}}^{g*} \ln[P_1(g)/P_2(g)]dg. \qquad [29]$$

The κ- and δ-type molecular interactions (Equations (28) and (29), respectively) result in modification of the criterion of Equation (26):

$$\frac{J_{\text{homo}}}{J_{\text{hetero}}} \approx \frac{n_v^{\text{eq}}}{N} e^{-R_2} e^{(\kappa-\delta)} \leq 1. \qquad [30]$$

The methods used to analyze Equation (26) are readily carried over to Equation (30). Positive values of $\delta - \kappa$ allow for the detection of smaller particles. Because measurements suggest that κ is typically quite small (i.e., several kT), almost any kind of molecular bonding between the substrate and the working fluid should allow for the detection of smaller particles than as predicted by Equation (26). The opposite tendency, requiring a larger particle sizes for the same detection efficiency, follows for repulsive interactions ($\delta < 0$)—including interactions of the type that manifest macroscopically as cases of imperfect wetting.

The results in this section show qualitatively and quantitatively how molecular interactions that lower (elevate) vapor pressure cause enhancement (reduction) of the nucleation rate. For the ternary organic acid/sulfuric acid/water systems discussed in Section 5, recent quantum chemical calculations point to strong organic acid–sulfuric acid hydrogen bonding as responsible for the stabilization of the critical complex and enhancement of the nucleation rate seen in laboratory measurements (Zhao et al. 2009).

7. SUMMARY AND DISCUSSION

In this paper, we presented theory and a graphical method for the analysis of homogeneous and heterogeneous nucleation barriers. The results reproduce the classical nucleation theory for the case that the droplet vapor pressure follows the Kelvin relation, while allowing interactions at the molecular scale that cause deviations in vapor pressure from the Kelvin result, and from the classical nucleation theory, to be formally included. Several nucleation theorems were shown to follow immediately from the graphical method, as does the Zeldovich factor, here related to the slope of the Kelvin curve at the critical nucleus size, that appears in expressions for homogeneous and heterogeneous nucleation rate.

Calculations based on MFPT kinetics were carried out and used as the benchmark to develop and test a new simplified expression for the MFPT and heterogeneous nucleation rate. Including (or not including in the case of heterogeneous nucleation) Courtney's $1/S$ correction and allowing for particle–vapor association at precritical levels of condensate yielded accuracies to within a few percentage points when compared with the MFPT results.

Criteria for guiding the selection of working fluids and operating conditions in order to optimize neutral particle detection were derived from a consideration of detection efficiency and a new metric for assessing heterogeneous nucleation—the signal-to-noise ratio. Corresponding states correlations, previously developed in the context of the homogeneous nucleation

theory, were shown to be applicable to heterogeneous nucleation and used to identify key scaling parameters and obtain results in a universal (material-independent) form. Detectability at minimal-seed-to-molecular-volume ratio, $v_{\text{seed}}/v_1 = n_{\text{seed}}^{\min}$, was shown to be favored for larger values of Ω/T, lower vapor concentration, n_v^{eq}, and molecular-level particle–working fluid interactions that lower vapor pressure relative to the Kelvin curve. In the latter case, to the extent such interactions (e.g., hydrogen bonding or antigen–antibody interactions) are favored and characteristically paired, highly selective methods for nanoparticle detection based on nucleation and growth should result. Future research should include extending the graphical method (or equivalent) to multi-component working fluids, more complete development of molecular-based approaches to the nucleation theory, and theory and experiment aimed at elucidating temperature dependence.

REFERENCES

Abraham, F. F. (1974). *Homogeneous Nucleation Theory*. Academic, New York, Chapter 5.

Becker, C., and Reiss, H. (1978). Estimation of Thermophysical Properties of a Large Polar Molecule and Application to Homogeneous Nucleation of *l*-Menthol. *J. Chem. Phys.*, 68:3585–3594.

Courtney, W. G. (1961). Remarks on Homogeneous Nucleation. *J. Chem. Phys.* 35:2249–2250.

Fernandez de la Mora, J. (2011). Heterogeneous Nucleation with Finite Activation Energy and Perfect Wetting: Capillary Theory versus Experiments with Nanometer Particles, and Extrapolations on the Smallest Detectable Nucleus. *Aerosol Sci. Technol.,* 45:543–554.

Fletcher, N. H. (1958). Size Effect in Heterogeneous Nucleation. *J. Chem. Phys.*, 29, 572–576.

Hale, B. N. (1992). The Scaling of Nucleation Rates. *Metallurgical Trans.*, 23A:1863–1868.

Hänggi, P., Talkner, P., and Borkovec, M. (1990). Reaction Rate Theory: Fifty Years after Kramers. *Rev. Mod. Phys.*, 62:251–341.

Iida, K., Stolzenburg, M. R., and McMurry, P. H. (2009). Effect of Working Fluid on Sub-2nm Particle Detection with a Laminar Flow Ultrafine Condensation Particle Counter. *Aerosol Sci. Technol.*, 43:81–96.

Jiang, J., Zhao, J., Chen, M., Eisele, F. L., Scheckman, J., Williams, B. J., et al. (2011). First Measurements of Neutral Atmospheric Cluster and 1–2 nm Particle Number Size Distributions during Nucleation Events. *Aerosol Sci. Technol.*, 45:ii–v.

Kashchiev, D. (1982). On the Relation between Nucleation Work, Nucleus Size, and Nucleation Rate. *J. Chem. Phys.*, 78:5098–5102.

Katz, J. L., Saltsburg, H., and Reiss, H. (1966). Nucleation in Associated Vapors. *J. Coll. Interface Sci.*, 21:560–568.

Magnusson, L.-E., Koropchak, J. A., Anisimov, M. P., Poznjakovskiy, V. M., and Fernandez de la Mora, J. (2003). Correlations for Vapor Nucleating Critical Embryo Parameters. *J. Phys. Chem. Ref. Data*, 32:1387–1410.

McGraw, R. (1981). A Corresponding States Correlation of the Homogeneous Nucleation Thresholds of Supercooled Vapors. *J. Chem. Phys.*, 75:5514–5521.

McGraw, R. (2001). Dynamics of Barrier Crossing in Classical Nucleation Theory. *J. Phys. Chem. B*, 105:11838–11848.

McGraw, R., and Laaksonen, A. (1996). Scaling Properties of the Critical Nucleus in Classical and Molecular-Based Theories of Vapor-Liquid Nucleation. *Phys. Rev. Letts.*, 76:2754–2757.

McGraw, R., and Lewis, E. R. (2009). Deliquescence and Efflorescence of Small Particles. *J. Chem. Phys.*, 131:194705–194719.

McGraw, R., and Wu, D. T. (2003). Kinetic Extensions of the Nucleation Theorem. *J. Chem. Phys.*, 118:9337–9347.

McGraw, R., and Zhang, R. (2008). Multivariate Analysis of Homogeneous Nucleation Rate Measurements. Nucleation in the p-Toluic Acid/Sulfuric Acid/Water System. *J. Chem. Phys.*, 128(6):064508–064517.

Rasmussen, D. H., and Babu, S. V. (1984). A Corresponding States Correlation for Nucleation from the Vapor. *Chem. Phys. Letts.*, 108:449–451.

Reiss, H., Marvin, D. C., and Heist, R. H. (1977). The Use of Nucleation and Growth as a Tool in Chemical Physics. *J. Coll. Interface Sci.*, 38:125–141.

Rudek, M. M., Fisk, J. A., Chakarov, V. M., and Katz, J. L. (1996). Condensation of a Supersaturated Vapor. XII. The Homogeneous Nucleation of the *n*-Alkanes. *J. Chem. Phys.*, 105:4707–4713.

Schobesberger, S., Winkler, P. M., Pinterich, T., Vrtala, A., Kulmala, M., and Wagner, P. E. (2010). Experiments on the Temperature Dependence of Heterogeneous Nucleation on Nanometer-Sized HaCl and Ag Particles. *Chem. Phys. Chem.*, 11:3874–3882.

Sipilä, M., K. Lehtipaloa, M. Attouib, K. Neitolaa, T. Petäjäae, P. P. Aaltoa, C. D. O'Dowd, et al. (2009). Laboratory Verification of PH-CPC's Ability to Monitor Atmospheric Sub-3 nm Clusters. *Aerosol Sci. Technol.*, 43:126–135.

Strey, R., Wagner, P. E., and Viisanen, Y. (1994). The Problem of Measuring Homogeneous Nucleation Rates and the Molecular Contents of Nuclei: Progress in the Form of Nucleation Pulse Measurements. *J. Chem. Phys.*, 98:7748–7758.

Vanhanen, J., Mikkilä, J., Lehtipalo, K., Sipilä, M., Manninen, H. E., Siivola, E., et al. (2011). Particle Size Magnifier for Nano-CN Detection. *Aerosol Sci. Technol.*, 45:533–542.

Vehkamäki, H., Määttänen, A., Lauri, A., Napari, I., and Kulmala, M. (2007). Technical Note: The Heterogeneous Zeldovich Factor. *Atmos. Chem. Phys.*, 7:309–313.

Vehkamäki, H., Määttänen, A., Lauri, A., Napari, I., Kulmala, M., Winkler, P., et al. (2007). Heterogeneous Multicomponent Nucleation Theorems for the Analysis of Nanoclusters. *J. Chem. Phys.*, 126:174707–174719.

Wedekind, J., Strey, R., and Reguera, D. (2007). New Method to Analyze Simulations of Activated Processes. *J. Chem. Phys.*, 126:134103–134115.

Winkler, P. M., Steiner, G., Vrtala, A., Vehkamäki, H., Noppel, M., Lehtinen, K. E. J., et al. (2008). Heterogeneous Nucleation Experiments Bridging the Scale from Molecular Ion Clusters to Nanoparticles. *Science*, 319:1374–1377.

Wölk, J., and Strey, R. (2001). Homogeneous Nucleation of H_2O and D_2O in Comparison: The Isotope Effect. *J. Phys. Chem. B*, 105:11683–11701.

Zhang, R., Suh, I., Zhao, J., Zhang, D., Fortner, E. C., Tie, X., et al. (2004). Atmospheric New Particle Formation Enhanced by Organic Acids. *Science*, 304:1487–1490.

Zhang, R., Wang, L., Khalizov, A. F., Zhao, J., Zheng, J., McGraw, R., et al. (2009). Formation of Nanoparticles of Blue Haze Enhanced by anthropogenic Pollution. *Proc. Natl. Acad. Sci.*, 106:17650–17654.

Zhao, J., Khalizov, A., Zhang, R., and McGraw, R. (2009). Hydrogen-Boding Interaction in Molecular Complexes and Clusters of Aerosol Nucleation Precursors. *J. Phys. Chem. A*, 113:680–689.